Research Article | Vol. 10, No. 1 | 1 Jan 2019 | BIOMEDICAL OPTICS EXPRESS 66

Biomedical Optics EXPRESS

Cellular-scale evaluation of induced photoreceptor degeneration in the living primate eye

SARAH WALTERS,[1,2,*] CHRISTINA SCHWARZ,[2,3] ROBIN SHARMA,[1,2,4] ETHAN A. ROSSI,[2,5] WILLIAM S. FISCHER,[6] DAVID A. DILORETO, JR.,[6] JENNIFER STRAZZERI,[2,6] DASHA NELIDOVA,[7] BOTOND ROSKA,[7] JENNIFER J. HUNTER,[1,2,6,8] DAVID R. WILLIAMS,[1,2,6] AND WILLIAM H. MERIGAN[2,6]

[1]*The Institute of Optics, University of Rochester, Rochester, NY, USA*
[2]*Center for Visual Science, University of Rochester, Rochester, NY, USA*
[3]*Currently with the Institute for Ophthalmic Research, University of Tübingen, Tübingen, Germany*
[4]*Currently with Facebook Reality Labs, Redmond, WA, USA*
[5]*Currently with the Departments of Ophthalmology & Bioengineering, University of Pittsburgh, Pittsburgh, PA, USA*
[6]*Flaum Eye Institute, University of Rochester, Rochester, NY, USA*
[7]*Friedrich Miescher Institute for Biomedical Research, Basel, Switzerland*
[8]*Department of Biomedical Engineering, University of Rochester, Rochester, NY, USA*
**swalter3@u.rochester.edu*

Abstract: Progress is needed in developing animal models of photoreceptor degeneration and evaluating such models with longitudinal, noninvasive techniques. We employ confocal scanning laser ophthalmoscopy, optical coherence tomography (OCT) and high-resolution retinal imaging to noninvasively observe the retina of non-human primates with induced photoreceptor degeneration. Photoreceptors were imaged at the single-cell scale in three modalities of adaptive optics scanning light ophthalmoscopy: traditional confocal reflectance, indicative of waveguiding; a non-confocal offset aperture technique visualizing scattered light; and two-photon excited fluorescence, the time-varying signal of which, at 730 nm excitation, is representative of visual cycle function. Assessment of photoreceptor structure and function using these imaging modalities revealed a reduction in retinoid production in cone photoreceptor outer segments while inner segments appeared to remain present. Histology of one retina confirmed loss of outer segments and the presence of intact inner segments. This unique combination of imaging modalities can provide essential, clinically-relevant information on both the structural integrity and function of photoreceptors to not only validate models of photoreceptor degeneration but potentially evaluate the efficacy of future cell and gene-based therapies for vision restoration.

© 2018 Optical Society of America under the terms of the OSA Open Access Publishing Agreement

1. Introduction

Since the advent of the ophthalmoscope in the nineteenth century [1], which provided the first *in vivo* view of the retina, efforts have continually focused on improving the non-invasive visualization of the many structures and cell classes in the retina. The use of adaptive optics in retinal imaging, particularly in scanning light ophthalmoscopy, substantially increased the lateral resolution that could be achieved [2,3]. Likewise, application of optical coherence tomography (OCT) in the living eye afforded a similarly impactful axial resolution increase, allowing individual layers of the retina to be clearly delineated [4–6]. Although these resolution increases revolutionized our ability to visualize many structures in the living retina and our understanding of changes that occur in retinal pathology, both AOSLO and OCT have traditionally relied upon light from an imaging source being directly backscattered to visualize structure. Recently, AOSLO imaging methods that use alternative strategies have

#345450 https://doi.org/10.1364/BOE.10.000066
Journal © 2019 Received 24 Sep 2018; revised 15 Nov 2018; accepted 15 Nov 2018; published 5 Dec 2018

Biomedical Optics EXPRESS

successfully increased contrast of traditionally hard-to-visualize retinal structures. A plethora of non-confocal imaging techniques, including split-detection [7–9], dark-field [8,10], and offset aperture [8,11,12], have enabled historically elusive retinal structures to come to light. Additionally, the intrinsic fluorescence of the retina, whether excited by one-photon [13,14] or two-photon [15,16] techniques, has been exploited to yield increased cellular contrast in several retinal layers.

Even though structural imaging remains instructive for studying cellular anatomy *in vivo*, it cannot definitely conclude the functional status of a cell. In fact, there is evidence that although a photoreceptor may not be detectable in confocal AOSLO imaging, that does not necessarily indicate lack of cellular function [17,18]. In such areas where photoreceptors appear dark, due to lack of waveguided light from the photoreceptors, structure can often be revealed with a non-confocal detection method [7,19,20]. Furthermore, AO microperimetry has shown that there can be remaining visual sensitivity in regions where cones are not visualized in confocal AOSLO imaging [18]. Likewise, abnormal reflectance of outer retinal layers in OCT does not necessarily indicate the functional status or even remaining structure of photoreceptors [19,21,22].

There are several objective methods that measure functional activity *in vivo* on a sub-retinal scale, such as multi-focal electroretinography [23,24], photopigment densitometry [25–28], and intrinsic signals [29–32]. Multi-focal electroretinography can measure functional activity of photoreceptors, but does not have sufficient resolution to distinguish the signal from individual photoreceptors. Photopigment densitometry and intrinsic signal measurements, while able to be performed on a cellular scale, can be highly variable and unreliable [28,29], though recent intrinsic signal measures of photoreceptor activity using OCT show promise [33,34]. AO microperimetry can accurately determine visual percepts from single cones [35,36], but psychophysical methods are not practical for determining the functional status of photoreceptors in animal models.

Intrinsic two-photon excited fluorescence (TPEF), on the other hand, has demonstrated potential for objectively measuring photoreceptor function on a cellular scale. The TPEF signal from photoreceptors, when measured as a function of time and in response to a visual stimulus, has been shown to be indicative of retinoid production [37,38]. As production of retinoids occurs most readily when the photoreceptor is actively responding to light, the time course of TPEF reflects functional activity of the photoreceptors [38,39]. All-*trans*-retinol, a molecular product of the visual cycle whose TPEF emission spectrum peaks around 490 nm [40,41], is thought to be the dominant source of time-varying fluorescence in the photoreceptor layer when using an excitation wavelength of 730 nm [37,38,41]. There are likely other contributors to the fluorescence signal, including the coenzymes NAD(P)H and FAD essential for cellular metabolism, which can be excited at 730 nm and emit in the visible range [42]. Although these are primarily contained in the inner segment and all-*trans*-retinol in the outer segment, the axial resolution of the AOSLO may preclude TPEF signal isolation from the inner or outer segments specifically [16]. Regardless of the specific fluorophore contributions, time course of TPEF has been shown to reliably quantify the amount of visual pigment expected to be bleached by a visual stimulus based on extraction of all-*trans*-retinol formation and clearance parameters [39]. Fluorescence from other endogenous fluorophores is not expected to change at the same time scales or with similar fractional quantity as all-*trans*-retinol [43,44]. When using an excitation wavelength of 900 nm, FAD in the inner segments and lipofuscin precursors such as A2E in the outer segments are the most likely contributors to the TPEF signal from the photoreceptors [16].

When applied to imaging of photoreceptors, the combination of confocal, non-confocal, and intrinsic TPEF AOSLO imaging techniques has the potential to inform both sub-cellular structure and visual cycle function. Non-confocal imaging has successfully been employed to visualize photoreceptors in both healthy and diseased retinas [7,12,19,20]. Intrinsic two-photon imaging has provided contrast in both inner and outer segments of photoreceptors

Biomedical Optics EXPRESS

[12,38] and has also successfully interrogated photoreceptor function [38,39,45]. Therefore, the combination of these imaging methods can be particularly useful when applied in cases of photoreceptor disruption, in which it may not be apparent from confocal reflectance AOSLO imaging and/or OCT whether photoreceptor structure is intact and the cells are functioning. In this study, we imaged non-human primates that have received a subretinal injection of a viral vector designed to locally damage photoreceptors [46] with confocal scanning laser ophthalmoscopy (cSLO) and OCT. In regions of photoreceptor disruption, we imaged the photoreceptor layer in three AOSLO imaging modalities: confocal reflectance, multioffset aperture, and TPEF. Additionally, we tracked the time course of TPEF from the photoreceptors to investigate functional activity. Finally, to validate our imaging results, we performed histology on one retina.

2. Methods

2.1 Animal preparation and subretinal injections

Three cynomolgus monkeys (*macaca fascicularis*) and one rhesus monkey (*macaca mulatta*) were injected subretinally with a viral vector designed to damage photoreceptors through targeting of microRNAs 182 and 183, which are strongly expressed in primate retina [46,47]. Monkeys will hereafter be described by an identification number, listed with demographical characteristics in Table 1. Animals were handled according to the protocols prescribed and approved by the University of Rochester's Committee on Animal Resources and in accordance with the ARVO Animal Statement for the Use of Animals in Ophthalmic and Vision Research.

An experienced retinal surgeon, one of the authors, performed all subretinal injections. Prior to injection, monkeys were anesthetized with 6 mg/kg of ketamine and 0.15 mg/kg of medetomidine. The eye and palpebral fissure were cleansed with 50% strength betadine/saline and rinsed with sterile saline. Healon OVD (Abbott Medical Optics Inc., Santa Ana, CA) or Genteal (Alcon Laboratories, Inc., Fort Worth, TX) was applied to maintain hydration, and a flat disposable vitrectomy lens (Volk Optical Inc., Mentor, OH) was placed on the eye. A lateral canthotomy was performed to increase the palpebral fissure. A 25 gauge valved trochar cannula was inserted into the eye with the appropriate entry system (Alcon Laboratories Inc., Fort Worth, TX) and a light pipe (Bausch and Lomb Millennium, cx9625, Bausch and Lomb Incorportated, Kingston-upon-Thames, United Kingdom) was inserted through it for surgical visibility. A 23 gauge valved trochar cannula (Alcon Laboratories Inc., Fort Worth, TX) was inserted into the opposite side of the eye and was used to place an extendible 41 gauge subretinal injection needle (Mfd. by D.O.R.C. International, Zuidland, The Netherlands, dist. by Dutch Ophthalmic, Exeter, NH) pre-loaded with virus. When the injector engaged the retina, a pneumatic picopump (World Precision Instruments, PV830, Sarasota, FL) was used to deliver a 20 pound-force per square inch, 2-4 second pulse in which 25 µl of virus was injected into the subretinal space.

Table 1. Summary of Non-Human Primate Subretinal Injections

Monkey ID	Species	Sex	Age	Location of bleb (w.r.t. fovea)	Bleb contact foveal region?
M1	*fascicularis*	F	4	superotemporal	Y
M2	*fascicularis*	M	6	superotemporal	Y
M3	*fascicularis*	F	6	superonasal	Y
M4	*mulatta*	M	11	superonasal	N

Blebs were placed in the central 30 degrees of the retina in the locations listed in Table 1. With the exception of monkey M4, the inferior edge of all subretinal blebs contacted the foveal region. Once the bleb was made, antibiotics (50-100µl of Vancomycin, 1mg/0.1ml and 50-100µl of Ceftazidime, 2mg/0.1ml) were injected into the intravitreal space. Pain relief was provided by prophylactic injections of 0.12 mg/kg of Buprenorphine SR (compounded by

Biomedical Optics EXPRESS

ZooPharm, Windsor, CO), given subcutaneously, as well as an intramuscular injection of 0.2 mg/kg of Meloxicam. Topical Maxitrol was placed on the eye and the monkeys were given an intramuscular injection of 0.2 mg/kg of Antisedan (Orion Pharma, Dhaka, Bangladesh) to reverse anesthesia. Retinal detachments due to the subretinal injections typically resolved within 24 hours.

2.2 Confocal SLO and OCT imaging

Changes in the retina following each injection were tracked with a confocal scanning laser ophthalmoscope (Spectralis HRA + OCT, Heidelberg Engineering, Heidelberg, Germany). For cSLO and OCT imaging, monkeys were anesthetized with 6 mg/kg of ketamine and 0.15 mg/kg medetomidine. Reversal of anesthesia upon completion of imaging was accomplished by an intramuscular injection of 0.2 mg/kg of Antisedan. Images of the subretinal bleb and surrounding region were obtained with a 30° square field-of-view in the following modalities: blue-light reflectance (BR; 488 nm), blue-light autofluorescence (BAF; excitation 488 nm, emission >510 nm), infrared reflectance (IR; 815 nm), and infrared autofluorescence (IRAF; excitation 786 nm, emission 810-840 nm). Spectral-domain OCT of the bleb and surrounding region was performed with line scans spaced 11 to 60 µm apart. cSLO and OCT imaging was performed prior to injection and once every one to four weeks post-injection. The total duration of follow-up imaging post-injection ranged from 8 to 30 months. During this period, cSLO images and OCT scans were visually inspected for changes in reflectivity or autofluorescence intensity. All OCT images are displayed on a logarithmic intensity scale.

2.3 Adaptive optics scanning light ophthalmoscopy

An ophthalmoscope designed for excitation and collection of two-photon fluorescence from the living primate eye was used to capture high resolution images of photoreceptors in the injected non-human primates. In preparation for imaging, macaques were anesthetized with ketamine (10-20 mg/kg) and midazolam (0.25 mg/kg) and secured in a stereotaxic device in ventral recumbency. After intubation, anesthesia was maintained by inhalation of isofluorane (1-5%). To reduce eye movements, paralysis was induced with intravenous vecuronium (40-80 µg/kg/hr) or rocuronium (200-400 µg/kg/hr), administered for up to a 6 hour period. Respiration was maintained by a ventilator during paralysis. Mydriasis and cycloplegia were induced with 1 to 2 drops each of phenylephrine hydrochloride (2.5%) and tropicamide (1%). A rigid gas permeable contact lens, coated with Genteal (Alcon, Fort Worth, TX, USA), was placed on the cornea to maintain hydration and correct base refractive error. The eye was held open with a lid retractor, and the animal's pupil was aligned to the exit pupil of the AOSLO.

Details of the system for AOSLO imaging have been described elsewhere [38]. Briefly, a laser diode (840 nm, 40 µW) was used for wavefront sensing and an ultrashort pulsed Ti:Sapphire laser (730 nm or 900 nm, 3.5 to 4.5 mW) for both reflectance imaging and excitation of intrinsic two-photon fluorescence. An additional source, a superluminescent diode (SLD; 796 nm, 200 µW), was focused at the same retinal plane as the Ti:Sapphire laser and was used to capture reflected light that provided high signal-to-noise imaging for image registration. Light levels listed are the average power over a 7.5 mm beam diameter incident on the cornea. Locations for AOSLO image acquisition were selected from regions of hyporeflectivity in the outer retina identified in OCT scans. These regions of interest were correlated to cSLO fundus images using custom MATLAB (Mathworks, Natick, MA) software to enable navigation to selected retinal locations using *en face* vasculature patterns. Videos of the photoreceptor mosaic at these locations of 1.1 (vertical) by 1.3 (horizontal) degrees in size were captured in three AOSLO modalities: confocal reflectance, multioffset aperture, and TPEF.

In the confocal reflectance modality, a photomultiplier tube (PMT) with a pinhole in the confocal position (Fig. 1(a)) captured directly backscattered light primarily emanating from the photoreceptor inner/outer segment boundary and the outer segment tip [48–50]. The

Biomedical Optics EXPRESS

AOSLO had two confocal reflectance detection channels, one for collecting reflected 796 nm light from the SLD using a 2.5 Airy disk diameter (ADD) pinhole, and one for collecting reflected 730 nm or 900 nm light from the Ti:Sapphire laser using either a 1.4 or 3.4 ADD pinhole. The confocal position of the pinhole in the Ti:Sapphire laser detection channel was optimized in the x, y, and z directions at the beginning of each imaging session via an automated algorithm that positioned the pinhole at the peak intensity of light backscattered from the primate retina [12,51].

The Ti:Sapphire laser detection channel was also used for multioffset imaging. This modality has been described elsewhere [12]. Briefly, the pinhole and PMT were sequentially displaced from the confocal position in opposite directions by either 4 or 8 ADD (Fig. 1(b)). This enabled capture of scattered light that was not primarily waveguided by the inner segments of the photoreceptors and thus was not focused to the confocal position in the detection channel [12]. Images from orthogonal non-confocal pinhole positions were combined in a manner similar to split detection by subtracting the two images and normalizing by their sum for each pixel, which provided visualization of the photoreceptor inner segments [7].

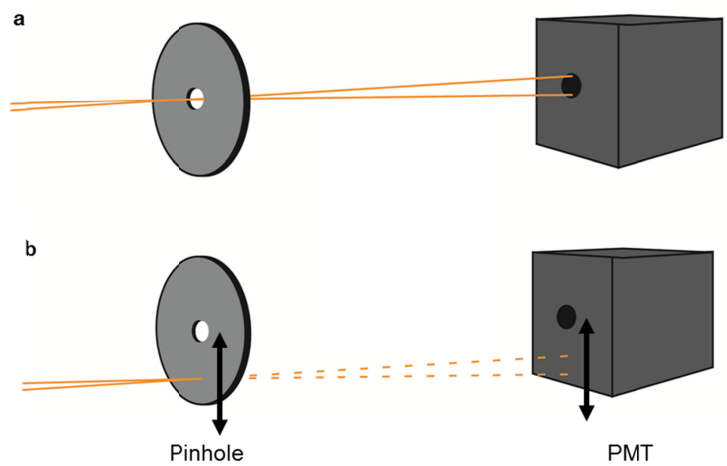

Fig. 1. AOSLO detection channel configurations for (a) confocal reflectance and (b) multioffset, where the pinhole and PMT are displaced from the confocal position.

TPEF was excited by the Ti:Sapphire laser and emitted fluorescence was collected with a PMT in a non-descanned configuration [16,38]. For 730 nm excitation, a filter pair (ET680sp-2P8 and E550sp-2p; Chroma Technology, Bellows Falls, VT) was employed to mitigate bleed-though from the laser and collect TPEF <550 nm. For 900 nm excitation, the 550 nm short pass filter was removed and TPEF was collected <680 nm.

TPEF and multioffset videos were collected in the same retinal location sequentially. During each acquisition, SLD confocal reflectance videos were simultaneously collected. Additionally, during TPEF imaging, a confocal reflectance video from the Ti:Sapphire laser was recorded. For each imaging modality, the axial focus of the laser was held constant for a given imaging location. Sinusoidal rectification of the video frames from resonant scanner motion was performed during image acquisition using a previously described method [52]. During post-processing, a custom video registration algorithm was employed to correct for movement of the primate eye due to heartbeat and respiration. A single frame from a SLD confocal reflectance video at a given retinal location was used as a reference to register the video frames of the TPEF, offset aperture, and Ti:Sapphire confocal reflectance videos, so that the videos from each modality were co-registered.

Biomedical Optics EXPRESS

2.4 Two-photon fluorescence time course

In healthy photoreceptors, the amount of all-*trans*-retinol in the outer segment is expected to increase after dark adaptation in response to a continuous light exposure from the 730 nm imaging laser, eventually plateauing as an equilibrium is reached between its formation and clearance [38,39]. The corresponding rise and plateau of the TPEF, therefore, is indicative of a normally functioning visual cycle. To evaluate the function of photoreceptors outside, along the margin of, and within areas of marked photoreceptor disruption, three different regions of interest (ROIs) in registered videos of TPEF collected from the photoreceptors were selected with ImageJ (NIH, Bethesda, MD) for analysis:

1) Normal-appearing photoreceptors in a contiguous mosaic were masked by manually segmenting a polygonal ROI which encompassed the region where the contiguous mosaic persisted.

2) Normal-appearing photoreceptors in a non-contiguous mosaic (i.e. within a region of low reflectivity) were segmented individually by drawing an elliptical mask around each photoreceptor, and individual ellipses were combined into a single ROI using a union operator.

3) Low-reflectivity photoreceptors were masked by hand-drawing a polygonal ROI which encompassed the region and then excluding the normal-appearing photoreceptors using an exclusive or operator.

The TPEF time course for each of the three ROIs was obtained by plotting the mean pixel value versus time for only the relevant masked portion of each registered TPEF video frame. Using MATLAB, the TPEF time course of the segmented data was fit with exponential functions of the form $y = \frac{\Delta F}{F} e^{-t/\tau} + 1$, where the fitting parameter τ is the time constant of TPEF increase and the fitting parameter $\frac{\Delta F}{F}$ is the relative increase in TPEF [45].

2.5 Histological preparation

Monkey M1 was euthanized for histological analysis of the bleb region 30 months after injection of the virus. The animal was perfused with 2.5% gluteraldehyde and 4% paraformaldehyde in 0.1 M phosphate buffer, and 100 µl of the same fixative was injected into the vitreous of the right eye, which was then enucleated. After the anterior segment was removed, the eye was immersion fixed for one hour at room temperature and then overnight at 4° C. Then the eye cup was trimmed to remove peripheral retina. The tissue was dehydrated through ascending concentrations of isopropanol and embedded in a glycol methacrylate plastic for soft tissue, Technovit H7100 (#14653, Electron Microscopy Sciences, Hatfield, PA, USA). The tissue and plastic polymerized in embedding molds (#70176-30, Electron Microscopy Sciences, Hatfield, PA, USA) at room temperature. A Microm HM355S rotary microtome (MICROM International GmbH, Germany) was used to section the tissue block at 2.5 µm. The sections were collected on drops of water on + charged slides and dried on a hot plate at 75°C. A two part stain was used to stain nuclei blue and cytoplasm pink. The stain was a modification by Griffin and Fahrenbach, Oregon Regional Primate Research Center, of [53]. A solution of methylene blue (#73881, Merck & Co. Inc., Rahway, NJ, USA) and azure II (#3112, Polysciences, Inc., Rahway, NJ, USA) was added to the slides dropwise on a hot plate at 75°C. After rinsing and drying, basic fuchsin (#F-98, Fisher Scientific Co., Fair Lawn, NJ, USA) was added in the same manner. Slides were again rinsed, dried, and coverslips applied. The retinal location of each section was determined by a comparison of anatomical features to those in the cSLO images to precisely align histology to

regions of AOSLO imaging. Sections were imaged with a light microscope in brightfield (BX53, Olympus, Tokyo, Japan) with a 60x oil immersion objective (UPlanSApo, Olympus, Tokyo, Japan).

3. Results

3.1 Evidence of damage to photoreceptors in confocal SLO and OCT imaging

Due to ocular inflammation as a result of the injections, interpretable cSLO images of the retina could not be obtained until 3–6 weeks after injection. After inflammation resolved, reflectance and autofluorescence images of the retina captured using the cSLO revealed that structural changes had occurred within the bleb region in all monkeys relative to their respective pre-injection condition.

Figure 2 shows representative images from M1 in each cSLO modality prior to and 28 weeks after injection. All monkeys in which the bleb contacted the foveal region developed a distinctive, patchy pattern of acute reflectance loss in BR images near the area where the bleb coincided with the foveal region. BAF was minimally affected for most monkeys within the bleb region (Fig. 2(h)), though M4 had more pronounced BAF reduction throughout the bleb (data not shown). Either slight hyperreflectivity or no change was observed within the bleb region in IR images (Fig. 2(b)). IRAF images showed reduced intensity in some areas within the bleb region (Fig. 2(d)); however, this observation may be confounded by the IRAF reduction that has been observed as a result of AOSLO imaging. IRAF reduction is slow to recover, taking up to several months to reach baseline values [54].

OCT B-scans taken through regions of patchy hyporeflectance in BR images revealed disruption localized to the outer retina (Fig. 3). Regions of reduced BR and OCT hyporeflective zones in the outer segments of the photoreceptors were well-correlated (Fig. 3). Reflectivity changes in BR and OCT remained stable and did not progress or recover after initial observation for the entire duration of follow-up imaging (8 to 30 months post-injection). Regions of reduced BR that correlated with OCT hyporeflective zones will be referred to here as affected regions. Regions of apparently normal BR and OCT will be referred to as unaffected regions.

3.2 Reduced waveguiding and TPEF in affected photoreceptors

Figure 4 shows AOSLO images from affected regions within the bleb at approximately 1 to 2 degrees eccentricity in the three monkeys in which the bleb contacted the foveal region. Photoreceptors appeared substantially darker in reflectance confocal AOSLO images of the affected region, suggesting impaired waveguiding in these cones compared to the surrounding, normally waveguiding cones (Fig. 4(a),(d),(g)). In these affected photoreceptors, TPEF signal at 730 nm excitation was reduced relative to unaffected cells (Fig. 4(b),(e),(h)). Although affected photoreceptors had minimal reflectance and TPEF, multioffset revealed that cellular structure remained in these regions, most likely arising from intact inner segments (Fig. 4(c),(f),(i)) [7]. The contrast of photoreceptor structure within these affected regions was notably greater in multioffset images.

Additional TPEF imaging at 900 nm excitation was performed in M1 and M2 (Fig. 5). In affected photoreceptors, there was a reduction of 75 ± 3% in TPEF signal excited by 730 nm when compared to unaffected photoreceptors (Fig. 5(a),(c)). TPEF signal excited by 900 nm was also diminished in affected photoreceptors, albeit by a lesser amount of 22.4 ± 1.3% (Fig. 5(b),(d)). However, distinct from TPEF images at 730 nm excitation, a cellular mosaic could still be clearly distinguished in affected regions in the TPEF images at 900 nm excitation.

In M1, M2, and M3, photoreceptors in affected regions were almost entirely cones given the proximity of the affected regions to the fovea. However, in M4, the affected region was further from the fovea, including both rod and cone photoreceptors (Fig. 6). Confocal reflectance images from approximately 5 degrees eccentricity revealed that many cones in the

Biomedical Optics EXPRESS

affected region were dark, whereas rods interspersed between the cones appeared bright (Fig. 6(a)). Just as in the aforementioned cases (Fig. 4), cones that had reduced waveguiding also had diminished TPEF (Fig. 6(b)). Again, multioffset revealed remaining structure for cones dark in reflectance and TPEF modalities (Fig. 6(c)). In general, rods appeared bright in both reflectance and TPEF; however, most were not clearly distinguishable in multioffset images, as has been noted in previous imaging of rods with split-detection [7].

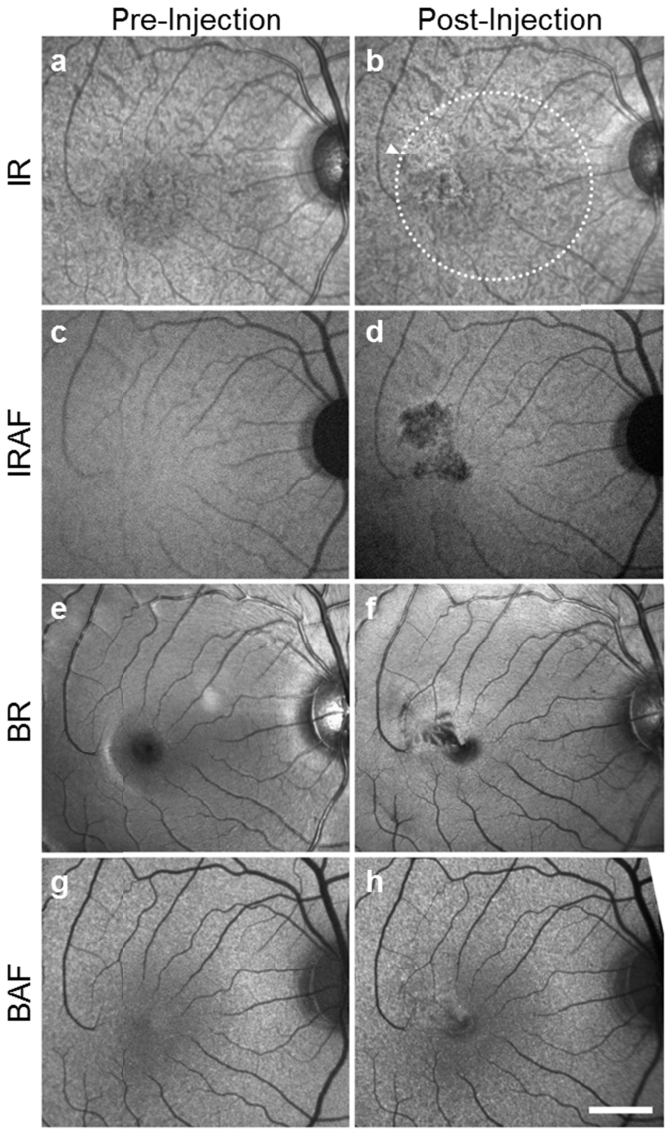

Fig. 2. cSLO images of M1 prior to (a,c,e,g) and 28 weeks after (b,d,f,h) subretinal injection of virus in four modalities: IR (a,b); IRAF (c,d); BR (e,f); BAF (g,h). In (b), white arrow denotes injection site, and white dashed circle the extent of the bleb. Scale bar: 1 mm.

Biomedical Optics EXPRESS

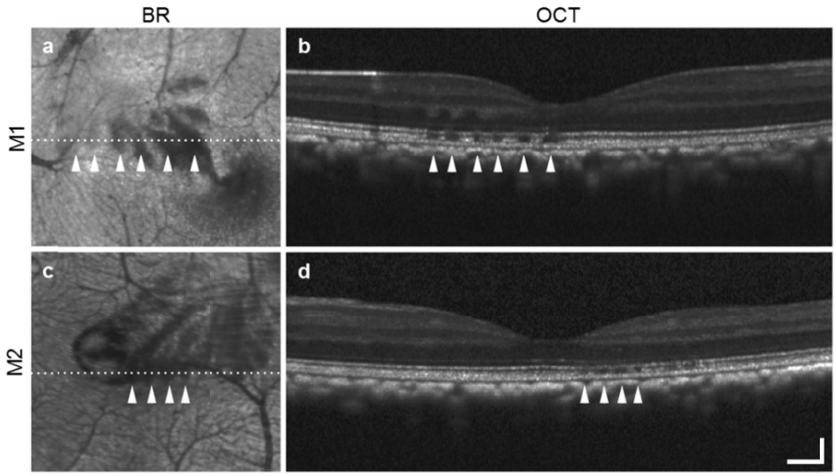

Fig. 3. cSLO (a,c) and corresponding OCT (b,d) of affected regions within the bleb for monkey M1 (a,b) and M2 (c,d). The dotted white line in cSLO images is indicative of the position of the OCT B-scans. White arrows mark positions of disruption in both the cSLO images and corresponding OCT B-scans. Scale bar: horizontal, 200 µm; vertical, 100 µm.

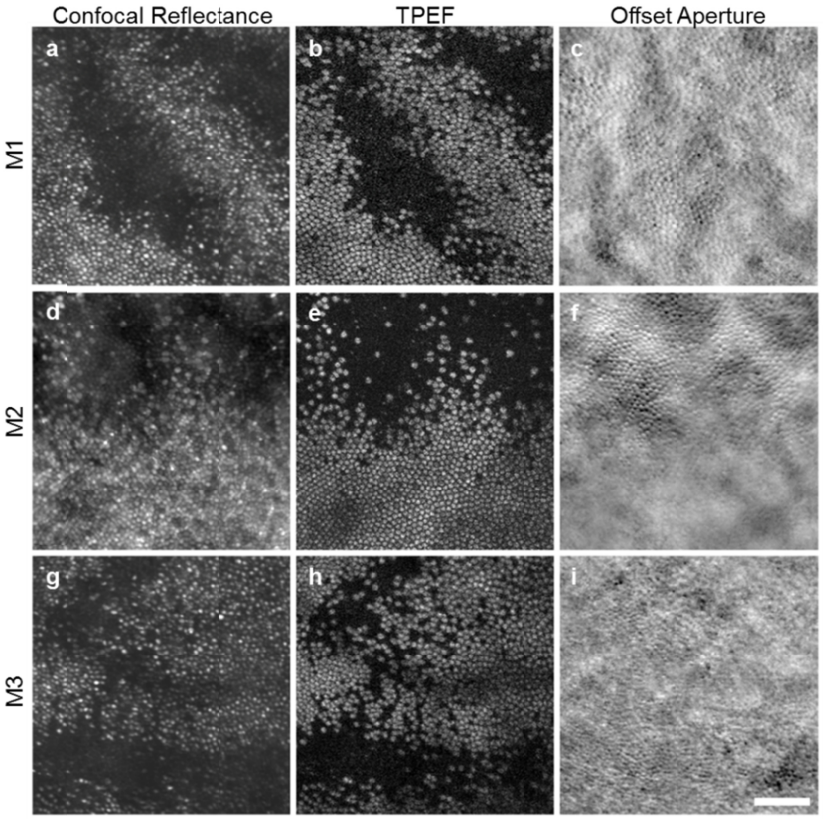

Fig. 4. AOSLO imaging of affected regions within the bleb of three monkeys. Images of the same location in three modalities are presented: 730 nm confocal reflectance (a,d,g), TPEF (b,e,h), and multioffset (c,f,i). Scale bar: 50 µm.

Biomedical Optics EXPRESS

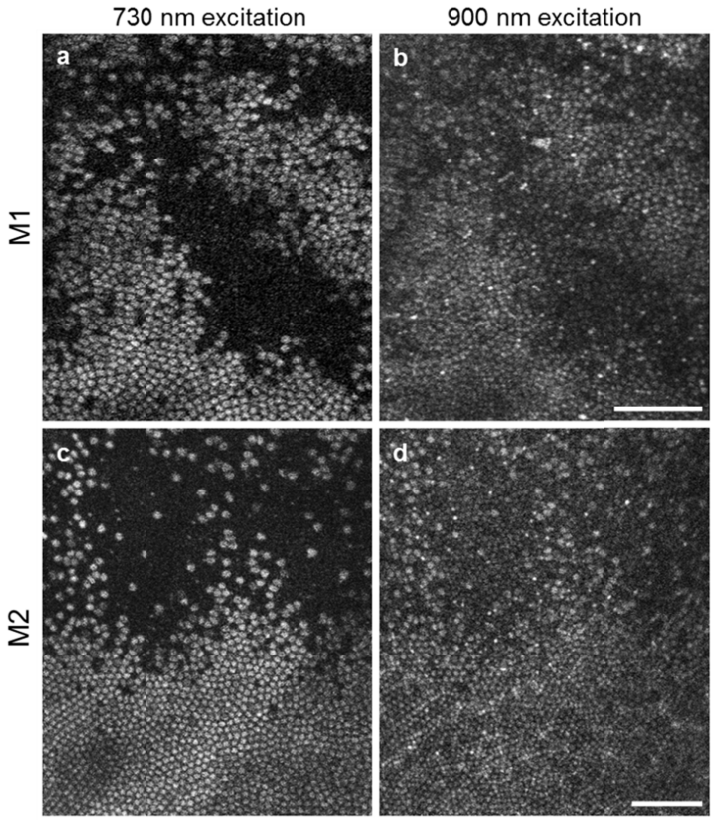

Fig. 5. TPEF imaging of affected regions in two monkeys at different excitation wavelengths. Images of the same location in each monkey are presented at 730 nm excitation (a, c) and 900 nm excitation (b, d). Scale bars: 50 µm.

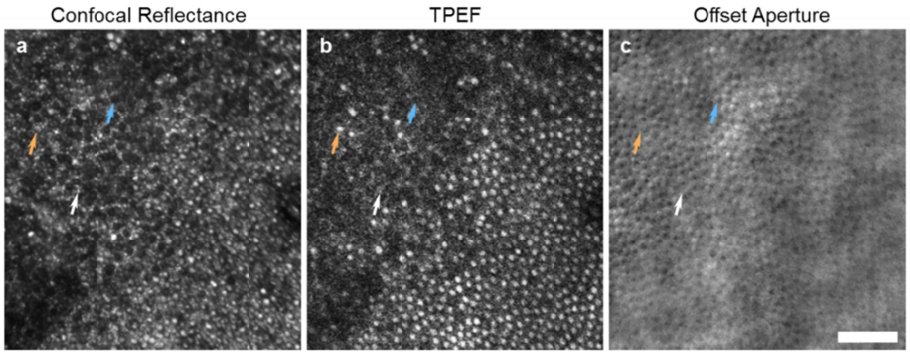

Fig. 6. AOSLO imaging of an affected region on the inferotemporal edge of the bleb in monkey M4, in three modalities: 730 nm confocal reflectance (a), TPEF (b), and multioffset (c). The orange arrow denotes a cone photoreceptor that appears to be waveguiding (a), is bright in TPEF (b), and has low contrast in multioffset (c). The blue arrow denotes a cone photoreceptor that appears dark in reflectance (a) and TPEF (b), but has high contrast in multioffset (c). The white arrow denotes a rod that is bright in reflectance (a) and TPEF (b), but could not be visualized in multioffset (c). Scale bar: 50 µm.

3.3 Altered time course of two-photon fluorescence in affected photoreceptors

The time course of photoreceptor TPEF intensity in response to the imaging laser has been previously characterized in healthy retina using the same system and imaging paradigm

Biomedical Optics EXPRESS

reported here, albeit with different powers of the Ti:Sapphire imaging laser [38,45]. The time course of TPEF was extracted for unaffected regions, affected regions, and normal-appearing photoreceptors interspersed within an affected region (Fig. 7). In unaffected regions with a contiguous photoreceptor mosaic in confocal reflectance and TPEF images, TPEF was shown to increase and plateau, indicating normal function of the visual cycle. Exponential fits to the TPEF time course in an unaffected region in M2 (Fig. 7(b)) yielded a time constant of 6.1 ± 0.3 s and relative TPEF increase of 0.44 ± 0.016. Photoreceptors that were near affected regions and were not part of a contiguous mosaic, but otherwise exhibited normal waveguiding, also produced a functional response to the imaging laser with a time constant of 5.4 ± 0.7 s and relative TPEF increase of 0.36 ± 0.03. In affected regions, where photoreceptors exhibited poor waveguiding, increase in TPEF at the onset of the imaging laser was much less evident, with a time constant of 39 ± 9 s and relative TPEF increase of 0.15 ± 0.012. Relative to unaffected photoreceptors, the longer time constant coupled with less relative increase in TPEF observed in affected photoreceptors indicates impaired function of the visual cycle.

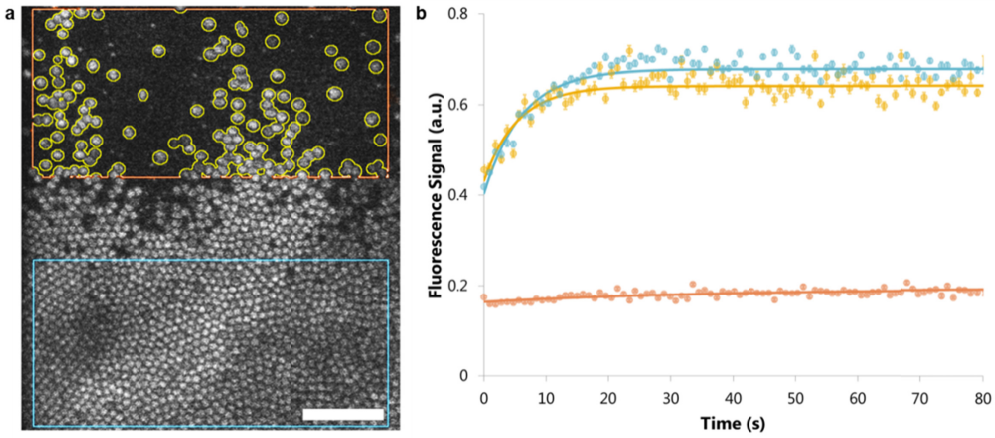

Fig. 7. The time course of TPEF for M2 in the same location as Fig. 4(d)-(f). Image segmentation is shown in (a), with the blue rectangle encompassing a normal region and the orange rectangle encompassing an affected region. Areas outlined in yellow are excluded from the affected region, and are plotted separately in their corresponding color in (b). Data points in (b) represent approximately 0.8 seconds of binned data of each of the regions in (a), with error bars representing standard error of the mean. Plotted lines in (b) are exponential fits to the data. Scale bar, 50 µm.

3.4 Damage to photoreceptor outer segments observed in histology of affected regions

Figure 8 presents histological sections through affected regions imaged with AOSLO imaging modalities in monkey M1. In general, regions designated as affected based on *in vivo* imaging modalities exhibited outer segment loss, while inner segments largely remained intact. In some affected regions, thinning of the outer nuclear layer was observed, as well as some loss of pigmentation in the retinal pigment epithelium (RPE).

Biomedical Optics EXPRESS

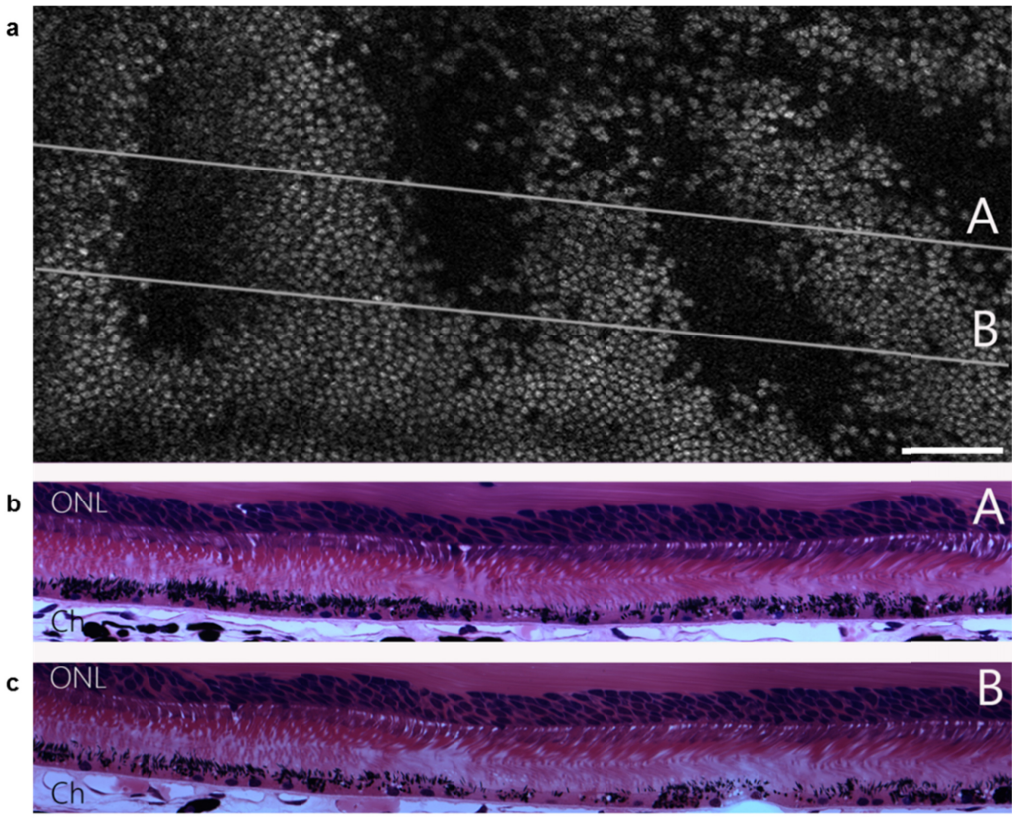

Fig. 8. Two histological sections (b and c) through an affected region in monkey M1, horizontally aligned to TPEF imaging at 730 nm excitation (a). Here, lines A and B denote angle of each histological section with respect to the *en face* imaging. ONL, outer nuclear layer; Ch, choroid. Scale bar, 50 μm.

4. Discussion

Confocal reflectance AOSLO has been previously shown to complement imaging with clinical instrumentation in evaluation of photoreceptor structure [55]. The healthy photoreceptor mosaic seen in AOSLO confocal reflectance images is enabled by waveguiding of light through the inner segment and the direct backscattering of light from both the photoreceptor inner/outer segment boundary and the outer segment tip [48–50]. As such, it is presumed that cones that are dark in confocal reflectance images, yet show inner segment structure in non-confocal images, are cones that could have compromised outer segment integrity [7]. In particular, poor photoreceptor waveguiding in confocal reflectance images due to a variety of diseases or ocular trauma typically corresponds with outer retinal disruptions in OCT [56,57]. The application of non-confocal AOSLO in such situations has revealed that even in regions where photoreceptors have reduced reflectance and outer retinal disruptions are visible in OCT, there can be remaining inner segment structure, lending to the technique an ability to present a clearer delineation of the bounds and extent of photoreceptor disruption [7]. In our model of induced photoreceptor degeneration in macaque, we find that outer retinal disruption in OCT does correlate well with poor photoreceptor waveguiding as revealed in confocal reflectance imaging, and furthermore, non-confocal multioffset imaging reveals remaining inner segment structure in those regions. The reduced TPEF signal in these cones adds specificity to this interpretation. All-*trans*-retinol, presumably the dominant time-varying fluorophore excited at 730 nm, is produced only in the outer segments of the cones.

At the very least, its drastic reduction would indicate that affected photoreceptors have inhibited production of all-*trans*-retinol. Further confirmation, and indication of functional activity, is provided through the time course of TPEF at 730 nm excitation. Unaffected photoreceptors exhibit a characteristic TPEF increase which has been shown to correlate with production of all-*trans*-retinol, demonstrative of a functioning visual cycle in response to continuous illumination from the 730 nm imaging laser [38]. In affected photoreceptors, a minimal and significantly slower increase was detected (Fig. 7). TPEF at 900 nm excitation yields additional evidence of the extent of inner and outer segment structure and function. Although the relative contribution of fluorophores is not yet known, it is likely primarily a combination of FAD, localized to the inner segments, and lipofuscin precursors such as A2E, localized to the outer segments. Remaining structure visualized at 900 nm excitation adds additional indication that inner segments are intact.

The implication of compromised outer segment integrity from the *in vivo* imaging is corroborated with definitive histological evidence from one retina. In affected regions of retina, many outer segments are indeed completely missing, while inner segments and photoreceptor cell bodies remain primarily intact, though the outer nuclear layer does thin slightly (Fig. 8). There is also a decrease in RPE pigmentation, consistent with the reduction in IRAF seen in cSLO imaging (Fig. 2(c),(d)) where signal is thought to originate from melanin within both the RPE and choroid [58]. Therefore, application of these three AOSLO imaging modalities holds great promise as a means to noninvasively and objectively evaluate not only inner and outer segment structure, but also functional status, of diseased or degenerating photoreceptors. Additionally, confirmation of outer segment but not inner segment loss provides evidence regarding the relative contribution of the outer and inner segments to the photoreceptor TPEF signal at both 730 and 900 nm excitation. It is apparent, with 730 nm excitation, that all-*trans*-retinol is indeed the dominant fluorophore in the photoreceptors, with relatively little contribution from inner segment TPEF, including NAD(P)H and FAD. At 900 nm excitation, the converse appears to be true: TPEF from inner segments is greater, likely due to FAD, while outer segment TPEF, likely due to lipofuscin precursors, is lesser.

In the present model of photoreceptor degeneration, there is seeming specificity of damage to cones, as rods within affected regions remain bright in confocal reflectance and do not exhibit drastic reduction of TPEF (Fig. 6). Cone outer segments appear vulnerable to a wide range of challenges to the outer retina such as autoimmune or infectious disorders [59]. Selective damage to cone outer segments, with preservation of inner segments and cone somas in the inner nuclear layer, has been reported in chronic progressive cone disorders such as achromatopsia [7,22] and reversible outer segment losses called multiple evanescent white dot syndrome, which may be caused by autoimmunity or infection [59]. In both disorders, substantial loss of cone outer segments produces complete blindness. In achromatopsia, loss of function in cones is due to a missense mutation of the cone alpha transducin and can be slightly progressive. On the other hand, white dot syndrome almost always shows recovery even without treatment, and recovery of even a modest number of outer segments, shown by adaptive optics imaging, may produce substantial visual recovery [59]. Retinal observations in achromatopsia patients are similar to the findings reported here, including regional changes in outer segments in OCT images, and preserved inner segments indicated by offset imaging [7]. Here, we also find that the damage does not appear to reverse, at least within the 8 to 30 month duration of our follow-up imaging.

Because cone outer segments are thought to be vulnerable to such general physiological stressors as autoimmunity and infection, we cannot determine if the cause of the outer segment damage observed here was identical to that in the Busskamp et al. study [46]. The present study also involved such challenges as the transient (< 24 hour) retinal detachment that subretinal injections produce, and although not expected to cause irreversible photoreceptor damage, its impact cannot be completely ruled out [60,61]. Additionally,

Biomedical Optics EXPRESS

adeno-associated viruses (AAVs) have been reported to cause immunotoxicity in the retina and it is possible that the cone outer segment loss was a consequence of AAV-mediated toxicity [62,63]. Nevertheless, although the mechanism of photoreceptor damage seen here has not been elucidated, this macaque model of photoreceptor degeneration may prove useful for testing of vision restoration methods. Certainly, challenges remain, such as the patchy, random nature of the degeneration, and also the seeming specificity of damage to cones. However, it is likely that visual function is impaired in affected regions, especially near the fovea where rods would not contribute to remaining visual sensitivity in the region. The remaining photoreceptor structure of inner segments and cell somas lends itself particularly well to cone rescue through optogenetic strategies [64].

Furthermore, although TPEF imaging with AOSLO has not yet been implemented in humans, it has potential to be an objective measure to inform the functional status of photoreceptors in damaged or degenerating retina [38,39,45]. Since the aforementioned diseases exhibit very similar phenotypes to the macaque model used here (i.e. an impairment of cone outer segments), TPEF, along with confocal reflectance and non-confocal AOSLO imaging, could be used to determine not only the amount of remaining photoreceptor structure in degenerating retina, but also provide an objective correlate of remaining visual sensitivity, all at the individual photoreceptor level. These three imaging AOSLO modalities could be used to noninvasively track longitudinal changes in retinal disease, as well as identify suitable candidates for gene therapy, optogenetics, or other vision restoration methods.

Funding

National Institutes of Health (NIH) (P30 EY001319, U01 EY025497, R01 EY022371, R01 EY021166); National Science Foundation (NSF) Graduate Research Fellowship Program (DGE-1419118); Research to Prevent Blindness, New York, NY (unrestricted grant to the University of Rochester Department of Ophthalmology).

Acknowledgments

The authors would like to thank the following people for their contributions to this project: Qiang Yang, for development of AOSLO imaging acquisition software and firmware and image registration software, as well as assistance with implementation of multioffset imaging; Amber Walker, Lee Anne Schery, and Louis DiVincenti, for care and handling of non-human primates and anesthesia during imaging experiments; Thurma McDaniel and Tracy Bubel, for preparation of histology; Brandi Hardy, for assistance in figure preparation; Drew Scoles and Juliette McGregor, for advice and input; Ge Song, for assistance with imaging sessions and data analysis; Alfredo Dubra and Kamran Ahmad, for development of adaptive optics control software; Martin Gira and Mark Ditz, for construction of the stereotaxic cart.

Disclosures

DRW: University of Rochester (P)

References

1. H. von Helmholtz, *Beschreibung eines Augen-Spiegels zur Untersuchung der Netzhaut im lebenden Auge* (A Förstner'sche Verlagsbuchhandlung, Berlin, Germany, 1851).
2. J. Liang, D. R. Williams, and D. T. Miller, "Supernormal vision and high-resolution retinal imaging through adaptive optics," J. Opt. Soc. Am. A **14**(11), 2884–2892 (1997).
3. A. Roorda, F. Romero-Borja, W. Donnelly Iii, H. Queener, T. Hebert, and M. Campbell, "Adaptive optics scanning laser ophthalmoscopy," Opt. Express **10**(9), 405–412 (2002).
4. D. Huang, E. A. Swanson, C. P. Lin, J. S. Schuman, W. G. Stinson, W. Chang, M. R. Hee, T. Flotte, K. Gregory, C. A. Puliafito, and et, "Optical coherence tomography," Science **254**(5035), 1178–1181 (1991).
5. E. A. Swanson, J. A. Izatt, M. R. Hee, D. Huang, C. P. Lin, J. S. Schuman, C. A. Puliafito, and J. G. Fujimoto, "In vivo retinal imaging by optical coherence tomography," Opt. Lett. **18**(21), 1864–1866 (1993).

Biomedical Optics EXPRESS

6. M. R. Hee, J. A. Izatt, E. A. Swanson, D. Huang, J. S. Schuman, C. P. Lin, C. A. Puliafito, and J. G. Fujimoto, "Optical coherence tomography of the human retina," Arch. Ophthalmol. **113**(3), 325–332 (1995).
7. D. Scoles, Y. N. Sulai, C. S. Langlo, G. A. Fishman, C. A. Curcio, J. Carroll, and A. Dubra, "In Vivo Imaging of Human Cone Photoreceptor Inner Segments," Invest. Ophthalmol. Vis. Sci. **55**(7), 4244–4251 (2014).
8. Y. N. Sulai, D. Scoles, Z. Harvey, and A. Dubra, "Visualization of retinal vascular structure and perfusion with a nonconfocal adaptive optics scanning light ophthalmoscope," J. Opt. Soc. Am. A **31**(3), 569–579 (2014).
9. A. Guevara-Torres, D. R. Williams, and J. B. Schallek, "Imaging translucent cell bodies in the living mouse retina without contrast agents," Biomed. Opt. Express **6**(6), 2106–2119 (2015).
10. D. Scoles, Y. N. Sulai, and A. Dubra, "In vivo dark-field imaging of the retinal pigment epithelium cell mosaic," Biomed. Opt. Express **4**(9), 1710–1723 (2013).
11. T. Y. P. Chui, D. A. Vannasdale, and S. A. Burns, "The use of forward scatter to improve retinal vascular imaging with an adaptive optics scanning laser ophthalmoscope," Biomed. Opt. Express **3**(10), 2537–2549 (2012).
12. E. A. Rossi, C. E. Granger, R. Sharma, Q. Yang, K. Saito, C. Schwarz, S. Walters, K. Nozato, J. Zhang, T. Kawakami, W. Fischer, L. R. Latchney, J. J. Hunter, M. M. Chung, and D. R. Williams, "Imaging individual neurons in the retinal ganglion cell layer of the living eye," Proc. Natl. Acad. Sci. U.S.A. **114**(3), 586–591 (2017).
13. D. C. Gray, W. Merigan, J. I. Wolfing, B. P. Gee, J. Porter, A. Dubra, T. H. Twietmeyer, K. Ahamd, R. Tumbar, F. Reinholz, and D. R. Williams, "In vivo fluorescence imaging of primate retinal ganglion cells and retinal pigment epithelial cells," Opt. Express **14**(16), 7144–7158 (2006).
14. J. I. W. Morgan, A. Dubra, R. Wolfe, W. H. Merigan, and D. R. Williams, "In vivo Autofluorescence imaging of the human and macaque retinal pigment epithelial cell mosaic," Invest. Ophthalmol. Vis. Sci. **50**(3), 1350–1359 (2009).
15. J. J. Hunter, B. Masella, A. Dubra, R. Sharma, L. Yin, W. H. Merigan, G. Palczewska, K. Palczewski, and D. R. Williams, "Images of photoreceptors in living primate eyes using adaptive optics two-photon ophthalmoscopy," Biomed. Opt. Express **2**(1), 139–148 (2011).
16. R. Sharma, D. R. Williams, G. Palczewska, K. Palczewski, and J. J. Hunter, "Two-photon autofluorescence imaging reveals cellular structures throughout the retina of the living primate eye," Invest. Ophthalmol. Vis. Sci. **57**(2), 632–646 (2016).
17. K. S. Bruce, W. M. Harmening, B. R. Langston, W. S. Tuten, A. Roorda, and L. C. Sincich, "Normal perceptual sensitivity arising from weakly reflective cone photoreceptors," Invest. Ophthalmol. Vis. Sci. **56**(8), 4431–4438 (2015).
18. Q. Wang, W. S. Tuten, B. J. Lujan, J. Holland, P. S. Bernstein, S. D. Schwartz, J. L. Duncan, and A. Roorda, "Adaptive optics microperimetry and OCT images show preserved function and recovery of cone visibility in macular telangiectasia type 2 retinal lesions," Invest. Ophthalmol. Vis. Sci. **56**(2), 778–786 (2015).
19. D. Scoles, J. A. Flatter, R. F. Cooper, C. S. Langlo, S. Robison, M. Neitz, D. V. Weinberg, M. E. Pennesi, D. P. Han, A. Dubra, and J. Carroll, "Assessing photoreceptor structure associated with ellipsoid zone disruptions visualized with optical coherence tomography," Retina **36**(1), 91–103 (2016).
20. E. J. Patterson, A. Kalitzeos, M. Kasilian, J. C. Gardner, J. Neitz, A. J. Hardcastle, M. Neitz, J. Carroll, and M. Michaelides, "Residual cone structure in patients with X-linked cone opsin mutations," Invest. Ophthalmol. Vis. Sci. **59**(10), 4238–4248 (2018).
21. L. W. Sun, R. D. Johnson, C. S. Langlo, R. F. Cooper, M. M. Razeen, M. C. Russillo, A. Dubra, T. B. Connor, Jr., D. P. Han, M. E. Pennesi, C. N. Kay, D. V. Weinberg, K. E. Stepien, and J. Carroll, "Assessing photoreceptor structure in retinitis pigmentosa and Usher syndrome," Invest. Ophthalmol. Vis. Sci. **57**(6), 2428–2442 (2016).
22. C. S. Langlo, E. J. Patterson, B. P. Higgins, P. Summerfelt, M. M. Razeen, L. R. Erker, M. Parker, F. T. Collison, G. A. Fishman, C. N. Kay, J. Zhang, R. G. Weleber, P. Yang, D. J. Wilson, M. E. Pennesi, B. L. Lam, J. Chiang, J. D. Chulay, A. Dubra, W. W. Hauswirth, and J. Carroll, "Residual foveal cone structure in CNGB3-associated achromatopsia," Invest. Ophthalmol. Vis. Sci. **57**(10), 3984–3995 (2016).
23. E. E. Sutter and D. Tran, "The field topography of ERG components in man-I. The photopic luminance response," Vision Res. **32**(3), 433–446 (1992).
24. D. C. Hood, J. G. Odel, C. S. Chen, and B. J. Winn, "The multifocal electroretinogram," J. Neuroophthalmol. **23**(3), 225–235 (2003).
25. A. Roorda and D. R. Williams, "The arrangement of the three cone classes in the living human eye," Nature **397**(6719), 520–522 (1999).
26. H. Hofer, J. Carroll, J. Neitz, M. Neitz, and D. R. Williams, "Organization of the human trichromatic cone mosaic," J. Neurosci. **25**(42), 9669–9679 (2005).
27. B. D. Masella, J. J. Hunter, and D. R. Williams, "Rod photopigment kinetics after photodisruption of the retinal pigment epithelium," Invest. Ophthalmol. Vis. Sci. **55**(11), 7535–7544 (2014).
28. B. D. Masella, J. J. Hunter, and D. R. Williams, "New wrinkles in retinal densitometry," Invest. Ophthalmol. Vis. Sci. **55**(11), 7525–7534 (2014).
29. K. Grieve and A. Roorda, "Intrinsic signals from human cone photoreceptors," Invest. Ophthalmol. Vis. Sci. **49**(2), 713–719 (2008).
30. J. Rha, R. S. Jonnal, K. E. Thorn, J. Qu, Y. Zhang, and D. T. Miller, "Adaptive optics flood-illumination camera for high speed retinal imaging," Opt. Express **14**(10), 4552–4569 (2006).

Biomedical Optics EXPRESS

31. J. Rha, B. Schroeder, P. Godara, and J. Carroll, "Variable optical activation of human cone photoreceptors visualized using a short coherence light source," Opt. Lett. **34**(24), 3782–3784 (2009).
32. P. Bedggood and A. Metha, "Variability in bleach kinetics and amount of photopigment between individual foveal cones," Invest. Ophthalmol. Vis. Sci. **53**(7), 3673–3681 (2012).
33. D. Hillmann, H. Spahr, C. Pfäffle, H. Sudkamp, G. Franke, and G. Hüttmann, "In vivo optical imaging of physiological responses to photostimulation in human photoreceptors," Proc. Natl. Acad. Sci. U.S.A. **113**(46), 13138–13143 (2016).
34. P. Zhang, R. J. Zawadzki, M. Goswami, P. T. Nguyen, V. Yarov-Yarovoy, M. E. Burns, and E. N. Pugh, "In vivo optophysiology reveals that G-protein activation triggers osmotic swelling and increased light scattering of rod photoreceptors," Proceedings of the National Academy of Sciences (2017).
35. W. S. Tuten, P. Tiruveedhula, and A. Roorda, "Adaptive optics scanning laser ophthalmoscope-based microperimetry," Optom. Vis. Sci. **89**(5), 563–574 (2012).
36. W. M. Harmening, W. S. Tuten, A. Roorda, and L. C. Sincich, "Mapping the perceptual grain of the human retina," J. Neurosci. **34**(16), 5667–5677 (2014).
37. C. Chen, E. Tsina, M. C. Cornwall, R. K. Crouch, S. Vijayaraghavan, and Y. Koutalos, "Reduction of all-trans retinal to all-trans retinol in the outer segments of frog and mouse rod photoreceptors," Biophys. J. **88**(3), 2278–2287 (2005).
38. R. Sharma, C. Schwarz, D. R. Williams, G. Palczewska, K. Palczewski, and J. J. Hunter, "In vivo two-photon fluorescence kinetics of primate rods and cones," Invest. Ophthalmol. Vis. Sci. **57**(2), 647–657 (2016).
39. R. Sharma, C. Schwarz, J. J. Hunter, G. Palczewska, K. Palczewski, and D. R. Williams, "Formation and clearance of all-trans-retinol in rods investigated in the living primate eye with two-photon ophthalmoscopy," Invest. Ophthalmol. Vis. Sci. **58**(1), 604–613 (2017).
40. R. R. Birge, J. A. Bennett, B. M. Pierce, and T. M. Thomas, "Two-photon spectroscopy of the visual chromophores. Evidence for a lowest excited 1Ag–like. pi.pi.* state in all-trans-retinol (vitamin A)," J. Am. Chem. Soc. **100**(5), 1533–1539 (1978).
41. M. W. Kaplan, "Distribution and axial diffusion of retinol in bleached rod outer segments of frogs (Rana pipiens)," Exp. Eye Res. **40**(5), 721–729 (1985).
42. S. Huang, A. A. Heikal, and W. W. Webb, "Two-photon fluorescence spectroscopy and microscopy of NAD(P)H and flavoprotein," Biophys. J. **82**(5), 2811–2825 (2002).
43. P. Lipton, "Effects of membrane depolarization on nicotinamide nucleotide fluorescence in brain slices," Biochem. J. **136**(4), 999–1009 (1973).
44. K. A. Kasischke, H. D. Vishwasrao, P. J. Fisher, W. R. Zipfel, and W. W. Webb, "Neural activity triggers neuronal oxidative metabolism followed by astrocytic glycolysis," Science **305**(5680), 99–103 (2004).
45. C. Schwarz, R. Sharma, W. S. Fischer, M. Chung, G. Palczewska, K. Palczewski, D. R. Williams, and J. J. Hunter, "Safety assessment in macaques of light exposures for functional two-photon ophthalmoscopy in humans," Biomed. Opt. Express **7**(12), 5148–5169 (2016).
46. V. Busskamp, J. Krol, D. Nelidova, J. Daum, T. Szikra, B. Tsuda, J. Jüttner, K. Farrow, B. G. Scherf, C. P. Alvarez, C. Genoud, V. Sothilingam, N. Tanimoto, M. Stadler, M. Seeliger, M. Stoffel, W. Filipowicz, and B. Roska, "miRNAs 182 and 183 are necessary to maintain adult cone photoreceptor outer segments and visual function," Neuron **83**(3), 586–600 (2014).
47. M. Karali, M. Persico, M. Mutarelli, A. Carissimo, M. Pizzo, V. Singh Marwah, C. Ambrosio, M. Pinelli, D. Carrella, S. Ferrari, D. Ponzin, V. Nigro, D. di Bernardo, and S. Banfi, "High-resolution analysis of the human retina miRNome reveals isomiR variations and novel microRNAs," Nucleic Acids Res. **44**(4), 1525–1540 (2016).
48. A. Pallikaris, D. R. Williams, and H. Hofer, "The reflectance of single cones in the living human eye," Invest. Ophthalmol. Vis. Sci. **44**(10), 4580–4592 (2003).
49. Y. Zhang, B. Cense, J. Rha, R. S. Jonnal, W. Gao, R. J. Zawadzki, J. S. Werner, S. Jones, S. Olivier, and D. T. Miller, "High-speed volumetric imaging of cone photoreceptors with adaptive optics spectral-domain optical coherence tomography," Opt. Express **14**(10), 4380–4394 (2006).
50. R. S. Jonnal, O. P. Kocaoglu, R. J. Zawadzki, S.-H. Lee, J. S. Werner, and D. T. Miller, "The cellular origins of the outer retinal bands in optical coherence tomography images," Invest. Ophthalmol. Vis. Sci. **55**(12), 7904–7918 (2014).
51. E. A. Rossi, P. Rangel-Fonseca, K. Parkins, W. Fischer, L. R. Latchney, M. A. Folwell, D. R. Williams, A. Dubra, and M. M. Chung, "In vivo imaging of retinal pigment epithelium cells in age related macular degeneration," Biomed. Opt. Express **4**(11), 2527–2539 (2013).
52. Q. Yang, L. Yin, K. Nozato, J. Zhang, K. Saito, W. H. Merigan, D. R. Williams, and E. A. Rossi, "Calibration-free sinusoidal rectification and uniform retinal irradiance in scanning light ophthalmoscopy," Opt. Lett. **40**(1), 85–88 (2015).
53. G. R. MacKay and M. L. Mead, "A simple dichromatic stain for plastic embedded tissues," in Proc. of 28th EMSA Meeting, 1970), 296–297.
54. B. D. Masella, D. R. Williams, W. S. Fischer, E. A. Rossi, and J. J. Hunter, "Long-term reduction in infrared autofluorescence caused by infrared light below the maximum permissible exposure," Invest. Ophthalmol. Vis. Sci. **55**(6), 3929–3938 (2014).
55. A. Roorda and J. L. Duncan, "Adaptive optics ophthalmoscopy," Annu. Rev. Vis. Sci. **1**(1), 19–50 (2015).

Biomedical Optics EXPRESS

56. J. A. Flatter, R. F. Cooper, M. J. Dubow, A. Pinhas, R. S. Singh, R. Kapur, N. Shah, R. D. Walsh, S. H. Hong, D. V. Weinberg, K. E. Stepien, W. J. Wirostko, S. Robison, A. Dubra, R. B. Rosen, T. B. J. Connor, Jr., and J. Carroll, "Outer retinal structure after closed-globe blunt ocular trauma," Retina **34**(10), 2133–2146 (2014).
57. J. Jacob, M. Paques, V. Krivosic, B. Dupas, A. Couturier, C. Kulcsar, R. Tadayoni, P. Massin, and A. Gaudric, "Meaning of visualizing retinal cone mosaic on adaptive optics images," Am. J. Ophthalmol. **159**(1), 118–123 (2015).
58. C. N. Keilhauer and F. C. Delori, "Near-infrared autofluorescence imaging of the fundus: visualization of ocular melanin," Invest. Ophthalmol. Vis. Sci. **47**(8), 3556–3564 (2006).
59. J. C. Horton, A. B. Parker, J. V. Botelho, and J. L. Duncan, "Spontaneous regeneration of human photoreceptor outer segments," Sci. Rep. **5**, 12364 (2015).
60. F. M. Penha, M. Maia, M. Eid Farah, A. H. Príncipe, E. H. Freymüller, A. Maia, O. Magalhães, Jr., and R. L. Smith, "Effects of subretinal injections of indocyanine green, trypan blue, and glucose in rabbit eyes," Ophthalmology **114**(5), 899–908 (2007).
61. D. H. Anderson, C. J. Guérin, P. A. Erickson, W. H. Stern, and S. K. Fisher, "Morphological recovery in the reattached retina," Invest. Ophthalmol. Vis. Sci. **27**(2), 168–183 (1986).
62. F. Mingozzi and K. A. High, "Immune responses to AAV vectors: overcoming barriers to successful gene therapy," Blood **122**(1), 23–36 (2013).
63. L. H. Vandenberghe, P. Bell, A. M. Maguire, C. N. Cearley, R. Xiao, R. Calcedo, L. Wang, M. J. Castle, A. C. Maguire, R. Grant, J. H. Wolfe, J. M. Wilson, and J. Bennett, "Dosage thresholds for AAV2 and AAV8 photoreceptor gene therapy in monkey," Science Translational Medicine **3**, 88ra54 (2011).
64. V. Busskamp, J. Duebel, D. Balya, M. Fradot, T. J. Viney, S. Siegert, A. C. Groner, E. Cabuy, V. Forster, M. Seeliger, M. Biel, P. Humphries, M. Paques, S. Mohand-Said, D. Trono, K. Deisseroth, J. A. Sahel, S. Picaud, and B. Roska, "Genetic reactivation of cone photoreceptors restores visual responses in retinitis pigmentosa," Science **329**(5990), 413–417 (2010).